Biosensors and Bioelectronics 133 (2019) 1–7

Contents lists available at ScienceDirect

Biosensors and Bioelectronics

journal homepage: www.elsevier.com/locate/bios

Microfluidic paper-based photoelectrochemical sensing platform with electron-transfer tunneling distance regulation strategy for thrombin detection

Jie Xue[a], Lina Zhang[b], Chaomin Gao[a,*], Peihua Zhu[a,*], Jinghua Yu[a]

[a] School of Chemistry and Chemical Engineering, University of Jinan, Jinan, Shandong 250022, PR China
[b] Shandong Provincial Key Laboratory of Preparation and Measurement of Building Materials, University of Jinan, Jinan 250022, PR China

ARTICLE INFO

Keywords:
Paper-based sensing platform
Photoelectrochemical
TiO_2
Electron-transfer tunneling distance regulation
Thrombin

ABSTRACT

This work reports a microfluidic paper-based photoelectrochemical (μ-PEC) sensing platform for thrombin (TB) detection with electron-transfer tunneling distance regulation (ETTDR) and aptamer target-triggering nicking enzyme signaling amplification (NESA) dual strategies. Specifically, paper-based TiO_2 nanosheets (PTNs) were prepared with an efficient hydrothermal process, serving as the direct pathway for the charge carriers transfer. When CeO_2-labeled hairpin DNA 3 (HP3) was closely located at the PTNs, the CeO_2-PTNs heterostructure was formed, which could great facilitate the photogenerated carries separation of CeO_2. In addition, with the aid of aptamer target-triggering NESA strategy, the input TB could be transducted to numerous output target of DNA (tDNA), achieving the goal of desirable signal amplification. In the presence of TB, the output tDNA could be further hybridized with HP3 and unfold its hairpin loop, which forced the CeO_2 away from the surface of PTNs and vanished the CeO_2-PTNs heterostructure, resulting in the obviously reducing of photocurrent signal. The as-designed sensing platform exhibited a linear range from 0.02 pM to 100 pM with a detection limit of 6.7 fM. Importantly, this μ-PEC sensing platform could not only realize the highly efficient TB detection, but also pave a luciferous way for the detection of other protein in bioanalysis.

1. Introduction

Cellulose paper, with the features of large specific surface area, high internal porosity, and rough surface, has been widely explored in the few years (Gao et al., 2018a; Zhang et al., 2017, 2018). Up to date, microfluidic paper-based analytical device possesses the superior merits including low-cost, portable, and high sensitive, has obtained considerable attention (Kokkinos et al., 2018; Li et al., 2018). Among them, paper-based photoelectrochemical (μ-PEC) sensing platform, which employs the complete separation of the detection signal and excitation source, providing high sensitivity with low background signal, has been achieved salient progress (Lan et al., 2017; Ju et al., 2014; Bellani et al., 2015; Sun et al., 2014; Chen et al., 2014). As known, the key factor to achieving high sensitivity in μ-PEC sensing platform is to produce a large photocurrent signal, namely, the photoelectric property of photoactive materials plays an important role in the analytical performance of sensing platform (Gao et al., 2018; Zhou et al., 2019). Varieties of semiconductors have been used to functionalize the cellulose paper, serving as the photoactive materials (Zhao et al., 2018; Kong et al., 2018a; Jiang et al., 2017; Liu et al., 2017). Among potential candidates, TiO_2 has been proved to be an excellent photoactive material due to its good biocompatibility, photoelectric activity, and chemical stability (Xu et al., 2012; Zhang et al., 2015; Li et al., 2017). Until now, paper based zero-dimension and two-dimension TiO_2 nanosheets have been successfully prepared (Stepien et al., 2013; Gao et al., 2018b). Notwithstanding, as for pure TiO_2, the photogenerated electron-hole pairs are apt to spontaneous recombination (Zheng et al., 2016; Gao et al., 2017), and only a fraction of them could migrate to the electrode surface and generate photocurrent, which affects the sensitivity of constructed sensing platform (Wang et al., 2019). Consequently, designing an ingenious strategy to promote efficient transfer of photogenerated carriers is highly demanded. Fortunately, the electron-transfer tunneling distance regulation (ETTDR) strategy has been proposed and ignited considerable research interest which could facilitate the separation of photogenerated carries. (Liu et al., 2008; Fan et al., 2003; Yang et al., 2015). With the aid of ETTDR strategy, a universal ratiometric PEC bioassay for ultrasensitive detection of microRNA has been fabricated (Zheng et al., 2017). By regulating the electron-transfer

* Corresponding authors.
E-mail addresses: chm_gaocm@163.com (C. Gao), chm_zhuph@ujn.edu.cn (P. Zhu).

https://doi.org/10.1016/j.bios.2019.03.022
Received 12 January 2019; Received in revised form 12 March 2019; Accepted 12 March 2019
Available online 13 March 2019

tunneling distance between photoactive material and sensing surface, the designed universal ratiometric PEC bioassay could realize sensitive detection of analyte. Inspired by aforementioned report, in this work, nanoceria (CeO_2) (Abdi et al., 2013; Kong et al., 2018b), a narrow band gap (2.67 eV) semiconductor with admirable light harvesting capacity and strong visible light excitation capability was utilized to fabrication the CeO_2-PTNs heterostructure by immobilizing CeO_2-labeled hairpin DNA 3 (HP3) on the surface of PTNs. In this way, the electron-transfer tunneling distance between CeO_2 and PTNs could be controlled. Meanwhile, the folded HP3 made the labeled CeO_2 move close to the surface of PTNs, leading to the formation of CeO_2-PTNs heterostructure and obviously increasing the photocurrent signal. What's more, PTNs could provide a direct pathway for photogenerated carriers, promoting the transfer of photogenerated carriers (Su et al., 2013). Importantly, this novel CeO_2-PTNs heterostructure has not been exploited in the paper based bioanalysis.

Nowadays, numerous aptamers with high-affinity and high-specific have been screened for the detection of target molecules (Xue et al., 2012). Compared with antibodies, aptamers offer several prominent advantages, such as owning stability and reusability, being easy-to-stock, and possessing widespread availability for almost any given subsistent protein (Choi et al., 2016; Yue et al., 2019). Nevertheless, one target could only trigger one target-aptamer binding interaction for generally, which limits the signal collection and detection sensitivity. In order to achieve high sensitivity, various aptamers based signal amplification strategies have been employed, such as rolling circle amplification (Wang et al., 2015; Yan et al., 2018), hybridization chain reaction (Wu et al., 2015), polymerase chain reaction (Yang and Ellington, 2008; Qi et al., 2018), and aptamer target-triggering nicking enzyme signaling amplification (NESA) (Li et al., 2014a). Among them, aptamer target-triggering NESA strategy has been extensively applied to construct PEC sensor due to its unique specificity for single-base mismatch detection, lower energy requirements, and excellent sensitivity for analytes (Xu et al., 2009; Li et al., 2011). Specifically, the nicking enzyme, as a special group of restriction endonucleases, was used to recognize specific sequences of a duplex DNA and cleave only one strand of it (Higgins et al., 2001). Besides, target-triggering NESA strategy can be carried out under an isothermal condition without other special instrumentation though nucleotide specific recognition technology and cyclic cleavage at the specific cleavage sites (Connolly and Trau, 2010). With those above-mentioned advantages, it is meaningful to integrated target-triggering NESA strategy with μ-PEC sensing platform to construct a sensitive sensor for bioanalysis.

In this work, a sensitive μ-PEC sensing platform based on aptamer target-triggering NESA and ETTDR strategies has been developed for thrombin (TB) detection for the first time. TB, as a type of serine endoprotease, has captured ongoing attention in recent years for its pivotal role in thrombosis, hemophilia, cardiovascular diseases and regulation of inflammation processes (Li et al., 2014b; Hao et al., 2018). Generally, excessive TB will cause thromboembolic diseases and low-volume of TB will give rise to excessive hemorrhage (Na et al., 2015). PTNs were prepared firstly via a simple hydrothermal process, subsequently, CeO_2-labeled HP3 was immobilized on the surface of PTNs, and an enhanced photocurrent signal was produced by CeO_2 in close proximity to PTNs. With the aid of target-triggering NESA strategy, the one input TB could be transducted to corresponding numerous output tDNA though nucleotide specific recognition technology and cyclic cleavage at the specific cleavage sites, simultaneously leading to a desirable efficient signal amplification. After that, the output tDNA were hybridized with HP3, the photocurrent signal dramatically decreased due to CeO_2 away from the PTNs. With such design, the as-prepared μ-PEC sensing platform exhibited good sensitivity, specificity, and reproducibility, which implies a great potential in clinical biomedicine detection of various proteins.

2. Experimental section

2.1. Design and preparation of the μ-PEC sensing platform

The preparation processes of the μ-PEC sensing platform were shown in Fig. S1. In details, Adobe illustrator CS6 software was used to design the shape patterns of μ-PEC sensing platform and the hydrophobic barrier was fabricated through wax-printing. After printing with a wax printer, the wax-printed paper (210 mm × 297 mm) was heated in an oven at 140 °C for 2 min to melt the wax, generating the hydrophobic barrier. Then, the wax-printed paper was cut into separate device and ready for PTNs growth. Finally, the Ag/AgCl reference electrode and carbon counter electrode were obtained through the screen-printed strategy.

2.2. Synthesis of the PTNs

Firstly, a layer of Ag was modified onto the paper working zone to endow it the desirable conductivity. Then, 0.35 g potassium titanium oxide oxalate dehydrate was added to 3 mL ultrapure water. After stirring for 10 min, 17 mL diethylene glycol was added into the above mixture with stirring for another 30 min. Finally, the mixture was transferred into Teflon-lined stainless steel autoclave, in which the paper substrate was placed with the conductivity side facing down. Subsequently, the autoclave was sealed and heated at 120 °C for 2 h. After cooling to room temperature, the sample was taken out, washed with ultrapure water and dried in ambient air.

2.3. Preparation of the CeO_2-labeled HP3

The CeO_2 was prepared according to the previously reports with slight modifications (Li et al., 2015, 2017), and the details were described in the Supplementary Materials. The CeO_2-labeled HP3 was obtained just like follows. Firstly, the CeO_2 was silylated with (3-aminopropyl) triethoxysilane. Then, 20 μL amino-functionalized CeO_2 was added into the mixture containing 20 μL of 10 mM N-(3-Dimethylaminopropyl)-N′-ethylcarbodiimide hydrochloride (EDC) and 10 mM N-hydroxysuccinimide (NHS). Subsequently, 20 μL of 4 μM HP3 was introduced to the above mixture and gently stirred for 2 h. The obtained solution was collected by wash-centrifugation cycles for three times, and further dispersed in phosphate buffered solutions (PBS) (pH 7.0) for following use.

2.4. Preparation of the magnetic beads (MB)-HP2

For preparation of the MB-HP2, 40 μL of MB was added into the mixture (20 μL) including 10 mM EDC and 10 mM NHS and stirred for 30 min. After washed with PBS, 20 μL of 4 μM HP2 was dropped into the mixture and continue stirring gently for 2 h. Under magnetic separation, the obtained MB-HP2 was washed and further redispersed in PBS (pH 7.0) for following use.

2.5. Aptamer target-triggering NESA strategy for TB detection

The aptamer target-triggering NESA strategy was performed as follows: the mixture containing 2 μM HP1 solution, 2 μM MB-HP2 solution, NEB buffer and different concentrations of TB was incubated at 37 °C for 1 h. Subsequently, 2 U μL^{-1} Nt.AlwI was added into the mixture and kept at 37 °C for 1.5 h. After that, the obtained mixture was heated at 80 °C for 20 min to deactivate Nt.AlwI and separated by magnet. Finally, the remaining solution containing different amount of tDNA was further used for immobilization on the surface of prepared paper working zone.

2.6. Construction and photoelectrochemical measurement of the μ-PEC sensing platform

Firstly, 20 μL of 0.05 mg mL^{-1} chitosan in 1.0% (*v/v*) acetic acid solution was casted onto the surface of paper working electrode and dried at room temperature. Then, 2.5% (*v/v*) glutaraldehyde (GLD) aqueous solution was added onto the surface of electrode and thoroughly washed to remove the physically absorbed GLD. After that, 20 μL of 2 μM CeO_2-labeled HP3 solution was dropped onto the paper working electrode for 2 h at 37 °C. Subsequently, 20 μL of 1 mM bovine serum albumin (BSA) solution was dropped on electrode surface at 37 °C for 1 h to block the nonspecific binding sites. Finally, the obtained solution containing different concentrations of tDNA was added onto the modified electrode at 37 °C for 1 h to unfold the HP3. What's more, the details about the photoelectrochemical measurement of the μ-PEC sensing platform were provided in Supplementary Materials.

3. Results and discussion

3.1. Characterizations of the PTNs and CeO_2

Firstly, the scanning electron microscopy (SEM), X-ray diffraction (XRD) and energy dispersive spectroscopy (EDS) were utilized to investigate the structural information of the PTNs (Fig. 1). As for the pure paper substrate, porous network of numerously intertwined cellulose fibers were observed, which could provide the paper substrate with large specific surface area (Fig. 1A). As shown in Fig. 1B and inset, the PTNs uniformly were coated on the surface of paper with vertically aligned configuration. In addition, the XRD was also carried out to study the crystallization property of the PTNs, as shown in Fig. 1C. As seen, in addition to the diffraction peaks of Ag-paper substrate, the new diffraction peaks of the PTNs with 2θ value around 25.4°, 48.1° and 54.6° could be clearly observed, which can be indexed to the (101), (200), (105) crystal plane of anatase TiO_2 (JCPDS No.21–1272). Furthermore, the EDS spectrum of PTNs clearly identified that the electrode was composed of Ti, O elements, which further confirmed the successful growth of PTNs (Fig. 1D). The EDS mapping (Fig. S2) can distinguish the distribution of the Ti and O elements.

The structural morphologies of CeO_2 were characterized with SEM, as presented in Fig. 2A. The SEM observation of CeO_2 exhibited a regular octahedron morphology with good dispersibility and smooth surface. From the magnified SEM image in the inset of Fig. 2A, it can be seen that the CeO_2 presents a diameter of approximately 50 nm. To further explore the crystal structure of CeO_2, XRD was studied as shown in Fig. 2B. The diffraction peaks located at 28.6, 33.1, 47.5, 56.4, 59.3, 69.3, 76.8 and 79.0 can be indexed to (111), (200), (220), (311), (222), (400), (331) and (420) crystal planes of body-centered cubic structure of CeO_2 (JCPDS No.34–0394). Notably, the X-ray photoelectron spectroscopy (XPS) of Ce 3d spectrum for CeO_2 (Fig. S3) indicated that the synthesized CeO_2 has only the characteristic peaks of Ce^{4+}. What's more, the ultraviolet-visible (UV–Vis) absorption spectrum of CeO_2 was also measured as shown in Fig. 2C. As can be seen, the light absorption edge of CeO_2 is located at about 460 nm, which demonstrated its desirable visible light adsorption ability.

3.2. Photoelectrochemical characterizations

To assess the photogenerated carries separation efficiency of sample, the steady-state photoluminescence (PL) was carried out with the excitation wavelength of 300 nm as shown in Fig. 3A. Evidently, the CeO_2 showed a high PL intensity at around 460 nm (curve a), which is due to the intrinsic luminescence of CeO_2 (Tian et al., 2013). An obvious decrease of the PL intensity was observed when formation of the CeO_2-PTNs heterostructure as compared with that of pure CeO_2 (curve b), indicating that the CeO_2-PTNs sample could effectively inhibit the recombination of photogenerated carries. To further investigate the

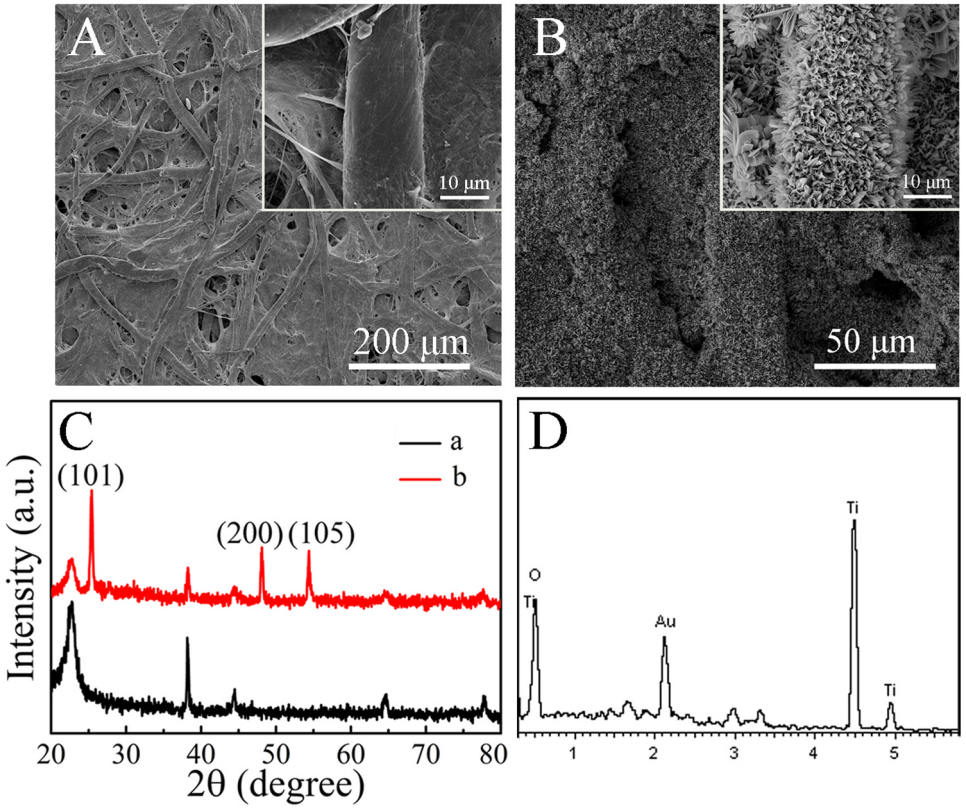

Fig. 1. (A) SEM images of paper substrate; inset, magnified SEM images of paper substrate. (B) SEM images of PTNs; inset, magnified SEM images of PTNs. (C) XRD pattern of (a) Ag-paper substrate and (b) PTNs; (D) EDS spectrum of PTNs.

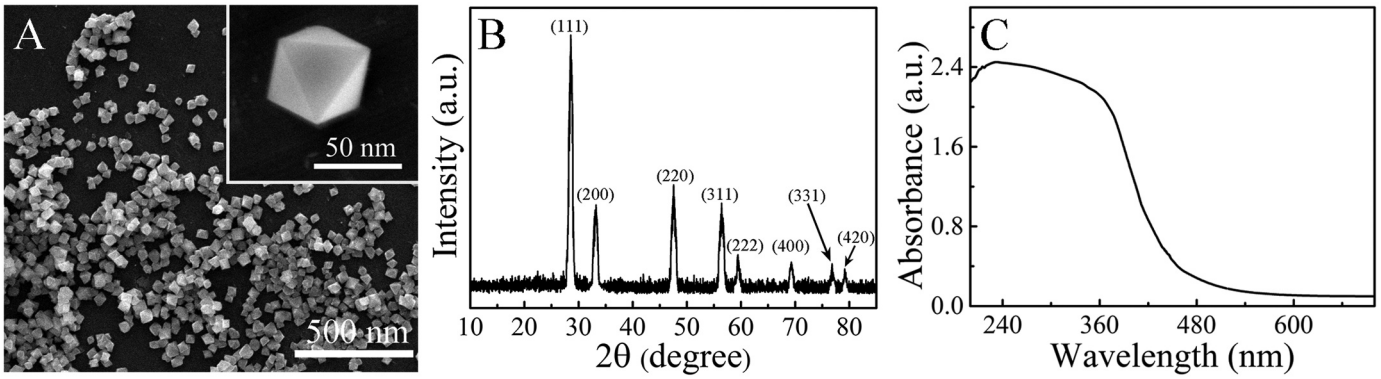

Fig. 2. (A) SEM images of CeO_2 (inset: magnified SEM image of CeO_2). (B) XRD pattern and (C) UV–Vis absorption spectra of CeO_2.

photo-induced carrier dynamics between PTNs and CeO_2, time-resolved photoluminescence (TRPL) was measured. As shown in Fig. 3B, the curves were fitted with the two exponential function: $F(t) = \Sigma A_i^{\tau/\tau i}$; i = 1, 2, where A_i is prefactor and τ_i is time constant. The fitted parameters of TRPL spectra were shown in Table S1. The CeO_2-PTNs sample decayed faster than the CeO_2, with PL lifetime of 5.08 ns and 3.28 for the CeO_2 and CeO_2-PTNs, respectively, further indicating that charge carriers within the CeO_2 could be extracted effectively by PTNs.

The photocurrent response during the stepwise fabrication processes of the sensing platform was also investigated as shown in Fig. 3C. As seen, the PTNs exhibited a relatively low photocurrent intensity since it could not be excited by 410 nm light (curve a). A noticeably increased photocurrent intensity was observed after the immobilization of CeO_2-labeled HP3 (curve b) due to the formation of the CeO_2-PTNs heterostructure. After BSA blocking (curve c), the photocurrent intensity decreased slightly due to the low electron transfer ability of immobilized BSA. After tDNA was bound on the surface of electrode, the photocurrent intensity decreased (curve d). The reason might be that the formed tDNA-HP3 complex could further block the electron transfer from AA to the surface of electrode as well as the disappearance of CeO_2-PTNs heterostructure due to the hybridization of tDNA and HP3. Consequently, all these results further suggested the successful construction of the μ-PEC sensing platform.

Electrochemical impedance spectroscopy (EIS) measurement was carried out to study the electron transfer resistance (R_{et}) of the PEC sensing platform in the stepwise fabrication process (Ge et al., 2017). Generally, the semicircular diameter of the EIS spectrum equals the R_{et}, which could reflect the electron transfer property of the electrodes (Ding et al., 2016). As shown in Fig. 3D, the R_{et} of PTNs exhibited a relatively small semicircle (curve a). After CeO_2-labeled HP3 immobilized onto the surface of PTNs (curve b), evidently increased of R_{et} was observed due to the low conductivity of DNA inhibited the electrons transfer. After blocking with BSA (curve c), the R_{et} increased, which may be due to the low conductivity of BSA. While the electrode was incubated with tDNA, the R_{et} further increased (curve d), indicating that the tDNA had hybridized with CeO_2-labeled HP3 probe. Accordingly, the gradually increased R_{et} showed that the proposed μ-PEC sensing platform had been successfully fabricated as expected.

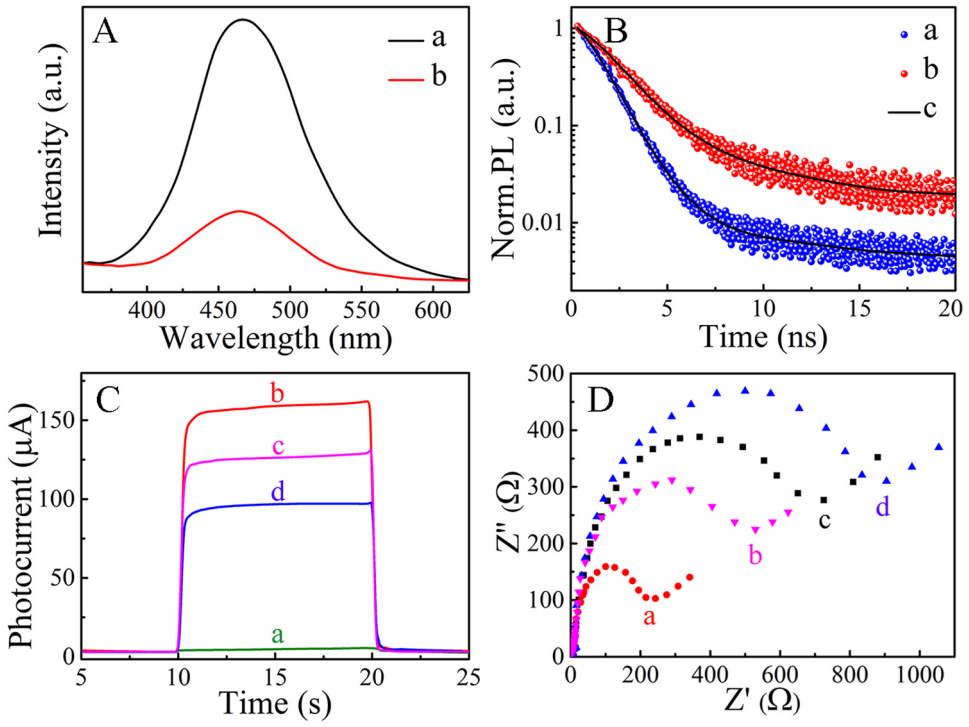

Fig. 3. (A) PL spectra of (a) CeO_2, (b) CeO_2/PTNs sample, λ_{Ex} = 300 nm. (B) TRPL spectra of (a) CeO_2, (b) PTNs/CeO_2. (C) Photocurrent response and (D) EIS spectra of (a) PTNs, (b) PTNs/CeO_2-labeled HP3, (c) PTNs/CeO_2-labeled HP3/BSA and (d) PTNs/CeO_2-labeled HP3/BSA/tDNA.

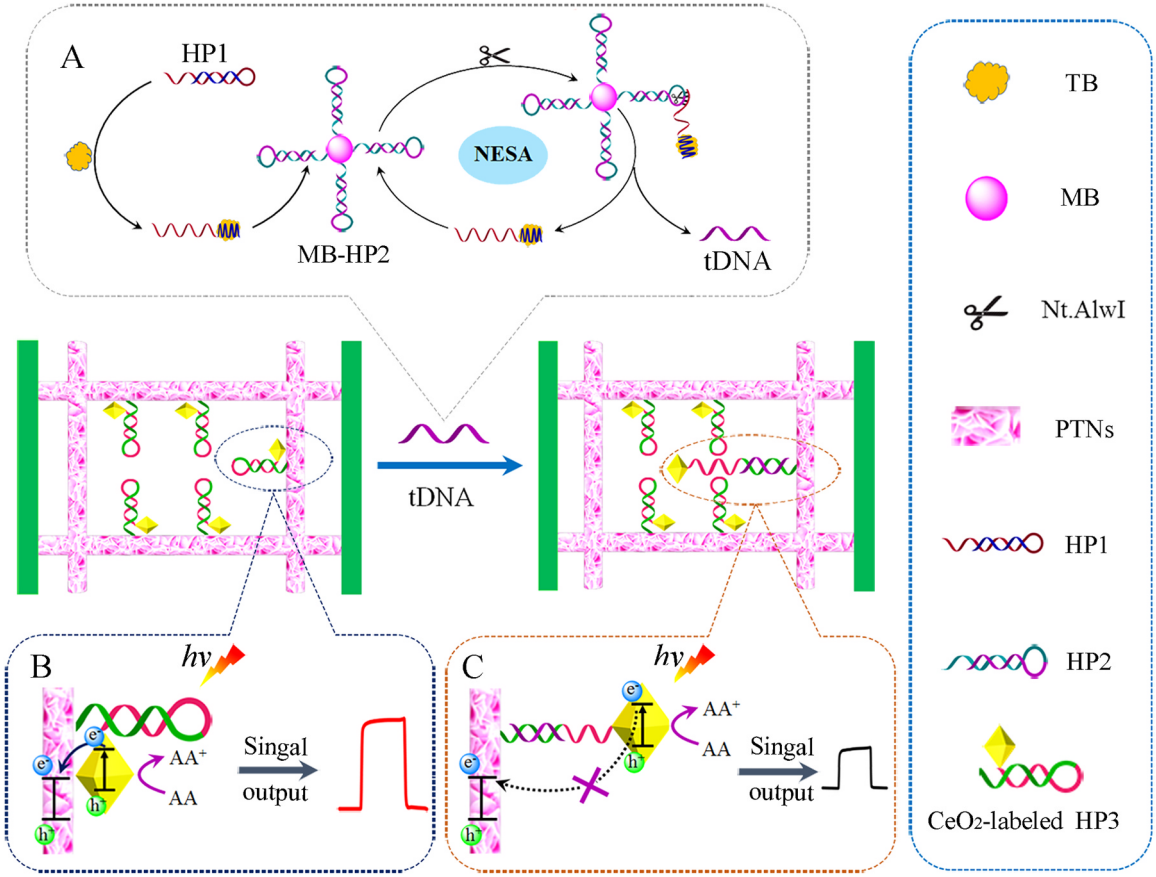

Scheme 1. Schematic illustration of the μ-PEC sensing platform. (A) The process of TB recognition and target-triggering NESA procedure. (B) The CeO_2-labeled HP3 were anchored on PTNs/paper working electrode and photocurrent-generating mechanism. (C) The autonomous release numerous secondary tDNA were hybridized with HP3 and photocurrent-decrease mechanism.

3.3. Possible working principle of the μ-PEC sensing platform

The working principle of the μ-PEC sensing platform was depicted in Scheme 1. Firstly, the PTNs were prepared via a hydrothermal process. After CeO_2-labeled HP3 anchored on the surface of PTNs, the photocurrent intensity was greatly enhanced, attributing to the formation of CeO_2-PTNs heterojunction. Under illumination, the electrons of CeO_2 were promptly excited from valence band (VB) to conduction band (CB), leaving behind holes in VB (Scheme 1B). Since the CB of PTNs is located lower than that of CeO_2, the PTNs can serve as an electron transfer layer, and the photogenerated electrons in the CB of CeO_2 could be promptly transferred into the CB of PTNs, resulting in a significant increase in photocurrent intensity. In the presence of TB, HP1 with aptamer of TB would specifically bond with TB to form HP1 @TB structure. The exposed segment of the formed HP1 @TB structure was then hybridized with MB-HP2. Subsequently, the HP1 @TB@MB-HP2 was digested by Nt.AlwI casing autonomous release numerous secondary tDNA for further hybridization reaction and the liberated HP1 @TB for new circulation-cleavage, which led to effective target signal conversion and amplification (Scheme 1A). Thereafter, these autonomous release numerous secondary tDNA could hybridize with CeO_2-labeled HP3 on the working electrode surface, which forced the CeO_2 away from the surface of PTNs, resulting in evidently declined photocurrent intensity (Scheme 1C). As a result, this μ-PEC sensing platform could achieve a specific and sensitive detection of TB.

3.4. Optimization of detection conditions

To obtain the optimal detection performance, several experiment conditions have been optimized. Firstly, the pH value of PBS was optimized (Fig. S4A). As seen, the maximum photocurrent response was obtained at pH 7.0. Therefore, the PBS with pH 7.0 was adopted for the following investigations. Subsequently, the concentration of Nt.AlwI was optimized (Fig. S4B). When the concentration of Nt.AlwI was increased into 2 U μL^{-1}, the maximum photocurrent intensity was obtained. Therefore, 2 U μL^{-1} was selected as the optimal concentration of Nt.AlwI. What's more, the incubation time of recycle process was also studied (Fig. S4C). With an increasing incubation time of recycle process, the photocurrent intensity gradually increased and nearly reached a plateau at 100 min. Therefore, 100 min was selected as the optimal incubation time of recycle process.

3.5. Analytical performance

Under the optimal conditions, the analytical performance of the developed μ-PEC sensing platform was investigated by detecting TB with varied concentrations. As displayed in Fig. 4A, a high photocurrent response was obtained in the absence of TB. After incubation with different concentrations of TB, part of CeO_2 was located away from the surface of PTNs, resulting in the decrease of photocurrent intensity. As seen from Fig. 4B, the photocurrent intensity decreased in a reduced linear relationship as the logarithm of TB concentration increased from 0.02 pM to 100 pM. The regression equation was $I = 78.4–28.35\ lgc_{TB}$ (pM), with the correlation coefficient of 0.9973. What is more, the limit of detection (S/N = 3) was estimated to be 6.7 fM, suggesting excellent detection sensitivity compared with the other reported methods (Table S2).

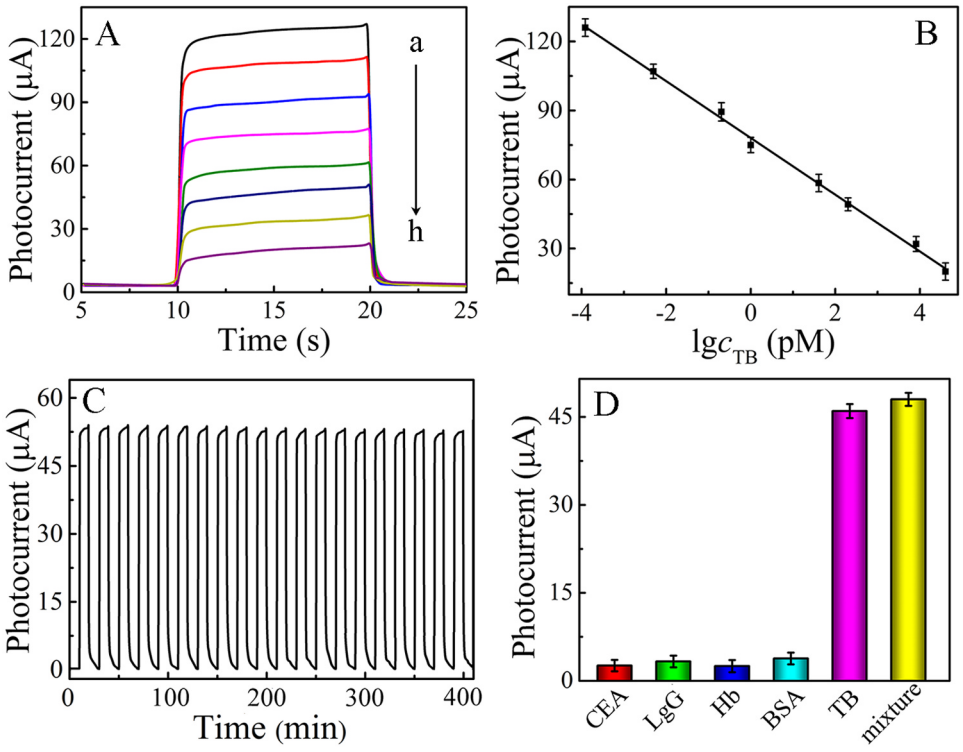

Fig. 4. (A) Photocurrent responses of the μ-PEC sensing platform with different concentrations of TB (the concentration was from a to h: 0.02, 0.1, 0.5, 1, 5, 10, 50, 100 pM). (B) the corresponding calibration curve for TB detection. (C) The stability evaluation of constructed μ-PEC sensing platform with the TB concentrations of 7 pM. (D) The selectivity evaluation of constructed μ-PEC sensing platform detection of TB against the interference proteins.

3.6. Stability, specificity, and reproducibility of the μ-PEC sensing platform

The stability of the as-prepared μ-PEC sensing platform was tested by using 7 pM of TB as an example and monitoring the photocurrent response of upon irradiation repeated every 10 s. After repeated irradiation program for 20 times over 400 s, there was no evident variation in photocurrent response (Fig. 4C), demonstrating the excellent stability of the prepared μ-PEC sensing platform. Furthermore, this sensor has acceptable long-term stability (Fig. S5).

The specificity was verified by comparing the results of 15 pM of TB and 100 pM of carcinoembryonic antigen (CEA), human IgG, hemoglobin (Hb), BSA (Fig. 4D). As seen, these interferences slightly cause the photocurrent intensity change. However, TB and the mixture containing TB and all above interferences obviously cause almost equal changes in photocurrent intensity, implying the high selectivity of μ-PEC sensing platform. The proposed selectivity coefficient (Table S3) also demonstrated the high selectivity of this method.

Moreover, the reproducibility of the developed sensing platform was estimated with interassay relative standard deviation (RSD). In the same condition, five batches of the sensing platforms were adopted to detect 10 nM TB. These five batches of sensing platforms depicted a similar photocurrent response with a RSD of 3.92%. Meanwhile, the same one sensing platform was measured for six times with RSD of 4.26%. Those results indicated that the sensing platform had a satisfactory reproducibility.

3.7. Real sample analysis

To further evaluate the real feasibility of prepared μ-PEC sensing platform, four human serum samples (obtained from Shandong Cancer Hospital, China) were measured by using the developed μ-PEC sensing platform and commercial enzyme-linked immunosorbent assay (ELISA) kit, respectively. All human serum samples were diluted 1000 times with PBS (pH 7.4) before the test. The summarized results (Table 1) were obtained by *t*-test statistical analysis. As seen, no significant different between these two methods was obtained because all *t* experimental value (t_{exp}) were less than *t* critical value (t_{crit}) ($t_{crit[0.05,4]}$ = 2.77), demonstrating the excellent potential practical application of μ-PEC sensing platform.

Table 1
Assay results of TB in human serum sample.

Sample (TB)	Method; concentration [mean ± SD, pM, n = 3]		t_{exp}
	μ-PEC sensing platform	ELISA kit	
1	3.83 ± 0.31	3.90 ± 0.26	0.29
2	8.12 ± 0.16	8.00 ± 0.10	1.07
3	15.00 ± 0.30	15.10 ± 0.60	0.26
4	23.23 ± 0.25	23.40 ± 0.40	0.61

4. Conclusions

In conclusion, a sensitive μ-PEC sensing platform was constructed based on the dual strategies of target-triggering NESA and ETTDR for the first time. The PTNs and CeO_2 were employed as the electron transporting material and photoactive material, respectively. Upon illumination, the photogenerated electrons of CeO_2 could be promptly transferred into PTNs, resulting in a significant increase of the photocurrent density. What's more, the target-triggering NESA strategy could produce abundant output tDNA, which further hybridize with HP3 to force the CeO_2 away from the electrode surface, resulting in the decrease of photocurrent intensity. By regulating the electron-transfer tunneling distance between PTNs and CeO_2, the designed μ-PEC sensing platform could realize sensitive detection of TB. With such design, this low-cost, portable, and sensitive μ-PEC sensing platform provides a feasible tool for TB detection and paves a new way in clinical applications of TB-related diseases, including clinical diagnosis, monitoring of disease progression, and other related subjects.

CRediT authorship contribution statement

Jie Xue: Conceptualization, Methodology, Investigation, Writing - original draft. **Lina Zhang:** Resources, Visualization, Data curation. **Chaomin Gao:** Writing - review & editing, Resources, Formal analysis. **Peihua Zhu:** Supervision, Funding acquisition. **Jinghua Yu:** Funding acquisition, Project administration.

Acknowledgements

This work was financial supports from the National Natural Science Foundation of China (21874055, 51872121, 21775055), the program for Taishan Scholer of Shandong Province (ts201712048), and the 111 Project of International Corporation on Advanced Cement-based Materials (No. D17001).

Declaration of competing interests

The authors declare that they have no known competing financial interests or personal relationships that could have appeared to influence the work reported in this paper.

Appendix A. Supporting information

Supplementary data associated with this article can be found in the online version at https://doi.org/10.1016/j.bios.2019.03.022.

References

Abdi, F.F., Han, L., Smets, A.H.M., Zeman, M., Dam, B., van de Krol, R., 2013. Nat. Commun. 4, 2195.
Bellani, S., Ghadirzadeh, A., Meda, L., Savoini, A., Tacca, A., Marra, G., Meira, R., Morgado, J., Di Fonzo, F., Antognazza, M.R., 2015. Adv. Funct. Mater. 25, 4531–4538.
Chen, G.H., Chen, W.Y., Yen, Y.C., Wang, C.W., Chang, H.T., Chen, C.F., 2014. Anal. Chem. 86, 6843–6849.
Choi, J.R., Hu, J., Tang, R., Gong, Y., Feng, S., Ren, H., Wen, T., Li, X., Wan Abas, W.A.B., Pingguan-Murphy, B., Xu, F., 2016. Lab Chip 16, 611–621.
Connolly, A.R., Trau, M., 2010. Angew. Chem. Int. Ed. 49, 2720–2723.
Ding, K., Zhang, X., Yang, P., Cheng, X., 2016. CrystEngComm 18, 8253–8261.
Fan, C., Plaxco, K.W., Heeger, A.J., 2003. Proc. Natl. Acad. Sci. USA 100, 9134–9137.
Gao, C.M., Xue, J.J., Zhang, L.N., Cui, K., Li, H., Yu, J.H., 2018a. Anal. Chem. 90, 14116–14120.
Gao, C., Yuan, S., Cui, K., Qiu, Z., Ge, S., Cao, B., Yu, J., 2018b. Sol. RRL 2, 1880175.
Gao, H.M., Zhang, D.Y., Yang, M.N., Dong, S., 2017. Sol. RRL 1, 1700183.
Ge, S., Lan, F., Liang, L., Ren, N., Li, L., Liu, H., Yan, M., Yu, J., 2017. ACS Appl. Mater. Interfaces 9, 6670–6678.
Hao, N., Hua, R., Chen, S., Zhang, Y., Zhou, Z., Qian, J., Liu, Q., Wang, K., 2018. Biosens. Bioelectron. 101, 14–20.
Higgins, L.S., Besnier, C., Kong, H., 2001. Nucleic Acids Res. 29, 2492–2501.
Jiang, D., Du, X., Zhou, L., Li, H., Wang, K., 2017. Anal. Chem. 89, 4525–4531.
Ju, Q., Uddayasankar, U., Krull, U., 2014. Small 10, 3912–3917.
Kokkinos, C.T., Giokas, D.L., Economou, A.S., Petrou, P.S., Kakabakos, S.E., 2018. Anal. Chem. 90, 1092–1097.
Kong, Q., Cui, K., Zhang, L., Wang, Y., Sun, J., Ge, S., Zhang, Y., Yu, J., 2018a. Anal. Chem. 90, 11297–11304.
Kong, Q., Wang, Y., Zhang, L., Xu, C., Yu, J., 2018b. Biosens. Bioelectron. 110, 58–64.
Lan, F., Liang, L., Zhang, Y., Li, L., Ren, N., Yan, M., Ge, S., Yu, J., 2017. ACS Appl. Mater. Interfaces 9, 37839–37847.
Li, C., Sun, Y., Djerdj, I., Voepel, P., Sack, C.C., Weller, T., Ellinghaus, R., Sann, J., Guo, Y., Smarsly, B.M., Over, H., 2017. ACS Catal. 7, 6453–6463.
Li, J., Yao, Q.H., Fu, H.E., Zhang, X.L., Yang, H.H., 2011. Talanta 85, 91–96.
Li, L., Lin, H., Lei, C., Nie, Z., Huang, Y., Yao, S., 2014a. Biosens. Bioelectron. 54, 42–47.
Li, L., Wang, Q., Feng, J., Tong, L., Tang, B., 2014b. Anal. Chem. 86, 5101–5107.
Li, L., Zheng, X., Huang, Y., Zhang, L., Cui, K., Zhang, Y., Yu, J., 2018. Anal. Chem. 90, 13882–13890.
Li, P., Zhou, Y., Zhao, Z., Xu, Q., Wang, X., Xiao, M., Zou, Z., 2015. J. Am. Chem. Soc. 137, 9547–9550.
Li, X., Zhu, L., Zhou, Y., Yin, H., Ai, S., 2017. Anal. Chem. 89, 2369–2376.
Liu, G., Wan, Y., Gau, V., Zhang, J., Wang, L., Song, S., Fan, C., 2008. J. Am. Chem. Soc. 130, 6820–6825.
Liu, Q., Huan, J., Hao, N., Qian, J., Mao, H., Wang, K., 2017. ACS Appl. Mater. Interfaces 9, 18369–18376.
Na, W., Liu, X., Wang, L., Su, X., 2015. Anal. Chim. Acta 899, 85–90.
Qi, H., Yue, S., Bi, S., Ding, C., Song, W., 2018. Biosens. Bioelectron. 110, 207–217.
Stepien, M., Saarinen, J.J., Teisala, H., Tuominen, M., Aromaa, M., Haapanen, J., Kuusipalo, J., Mäkelä, J.M., Toivakka, M., 2013. Langmuir 29, 3780–3790.
Su, F., Wang, T., Lv, R., Zhang, J., Zhang, P., Lu, J., Gong, J., 2013. Nanoscale 5, 9001–9009.
Sun, G., Wang, P., Ge, S., Ge, L., Yu, J., Yan, M., 2014. Biosens. Bioelectron. 56, 97–103.
Tian, J., Sang, Y., Zhao, Z., Zhou, W., Wang, D., Kang, X., Liu, H., Wang, J., Chen, S., Huang, H., 2013. Small 9, 3864–3872.
Wang, K., Liao, J., Yang, X., Zhao, M., Chen, M., Yao, W., Tan, W., Lan, X., 2015. Biosens. Bioelectron. 63, 172–177.
Wang, M., Yin, H., Zhou, Y., Sui, C., Wang, Y., Meng, X., Waterhouse, G.I.N., Ai, S., 2019. Biosens. Bioelectron. 128, 137–143.
Wu, D., Xin, X., Pang, X., Pietraszkiewicz, M., Hozyst, R., Sun, X.G., Wei, Q., 2015. ACS Appl. Mater. Interfaces 7, 12663–12670.
Xu, M., Da, P., Wu, H., Zhao, D., Zheng, G., 2012. Nano Lett. 12, 1503–1508.
Xu, W., Xue, X., Li, T., Zeng, H., Liu, X., 2009. Angew. Chem. Int. Ed. 48, 6849–6852.
Xue, L., Zhou, X., Xing, D., 2012. Anal. Chem. 84, 3507–3513.
Yan, Y., Li, J., Li, W., Wang, Y., Song, W., Bi, S., 2018. Nanoscale 10, 22456–22465.
Yang, L., Ellington, A.D., 2008. Anal. Biochem. 380, 164–173.
Yang, Y., Huang, J., Yang, X., Quan, K., Wang, H., Ying, L., Xie, N., Ou, M., Wang, K., 2015. J. Am. Chem. Soc. 137, 8340–8343.
Yue, S., Song, X., Song, W., Bi, S., 2019. Chem. Sci. 10, 1651–1658.
Zhang, R., Cheng, X., Hou, P., Ye, Z., 2015. Constr. Build. Mater. 81, 35–41.
Zhang, Y., Li, L., Zhang, L., Ge, S., Yan, M., Yu, J., 2017. Nano Energy 31, 174–182.
Zhang, Y., Zhang, L., Cui, K., Ge, S., Cheng, X., Yan, M., Yu, J., Liu, H., 2018. Adv. Mater. 30, 1801588.
Zhao, Y., Tan, L., Gao, X., Jie, G., Huang, T., 2018. Biosens. Bioelectron. 110, 239–245.
Zheng, L.X., Han, S.C., Liu, H., Yu, P.P., Fang, X.S., 2016. Small 12, 1527–1536.
Zheng, Y.N., Liang, W.B., Xiong, C.Y., Zhuo, Y., Chai, Y.Q., Yuan, R., 2017. Anal. Chem. 89, 9445–9451.
Zhou, Y., Yin, H., Sui, C., Wang, Y., Ai, S., 2019. Chem. Eng. J. 357, 94–102.